



---

Newport News, VA

***Hall D Tracking and PID Review***



Physics and Detector Performance Metrics

GlueX-doc-999-v7

# 1 Introduction

We start this report on the GLUEX detector by discussing the physics goals of the GLUEX project, which focuses on mapping the spectrum of gluonic excitations, starting with exotic hybrid mesons produced using a beam of 9 GeV linearly polarized photons. We show that the search for exotic mesons depends critically on detecting and measuring the four-momenta of charged particles and photons resulting from the decays of photoproduced mesons. As will be discussed in this report, the majority of the final states to be studied in GLUEX involve a combination of both charged particles and photons. Thus, the design of the GLUEX detector has taken a unified approach to assure good acceptance and resolution for detection of all particles. We then review the existing photoproduction data, where the extremely low statistics and limited capabilities (for neutrals) of older experiments indicate that very little is known about the physics to be studied in GLUEX [1].

The detector requirements on GLUEX are driven by the need to identify exclusive reactions in order to perform the amplitude analysis that will extract meson quantum numbers,  $J^{PC}$ , and the need to be sensitive to a variety of meson decay modes. Generally speaking, an amplitude analysis needs a large and uniform acceptance detector with resolution sufficient for cleanly separating final states. This reduces background leakage into the reactions of interest. In order to demonstrate that the GLUEX experiment will be capable of carrying out its physics goals, we compare the capabilities of GLUEX with the successful Brookhaven E852 experiment. We show that for the kinematic quantities of interest in the GLUEX analyses, the performance is GLUEX is very comparable to E852. With similar statistics as E852, the search in for exotic mesons can be carried out in GLUEX at least as well as E852. This coupled with the both the sparseness of existing photoproduction data, and the much higher statistics expected in GLUEX, leads us to conclude that GLUEX has an excellent chance of discovering and mapping exotic mesons if they exist.

In the latter part of this report are shown the underlying detector performances that lead to the above conclusions. For much of the physics of exotic mesons, being able to separate pions from protons is necessary. Information of the individual particle identification systems as well as information on more sophisticated global analyses is discussed. The separation of pions and protons will be very good in GLUEX, while the clean identification of kaons will be difficult using the existing particle identification detectors alone. This report also summarizes information on the performance of the tracking chambers that are used to reconstruct charged particles in GLUEX. This includes the information on how the position resolution of the chambers translates into momentum resolution and a summary of the expected kinematics in GLUEX and how it maps onto the tracking elements of the detector.

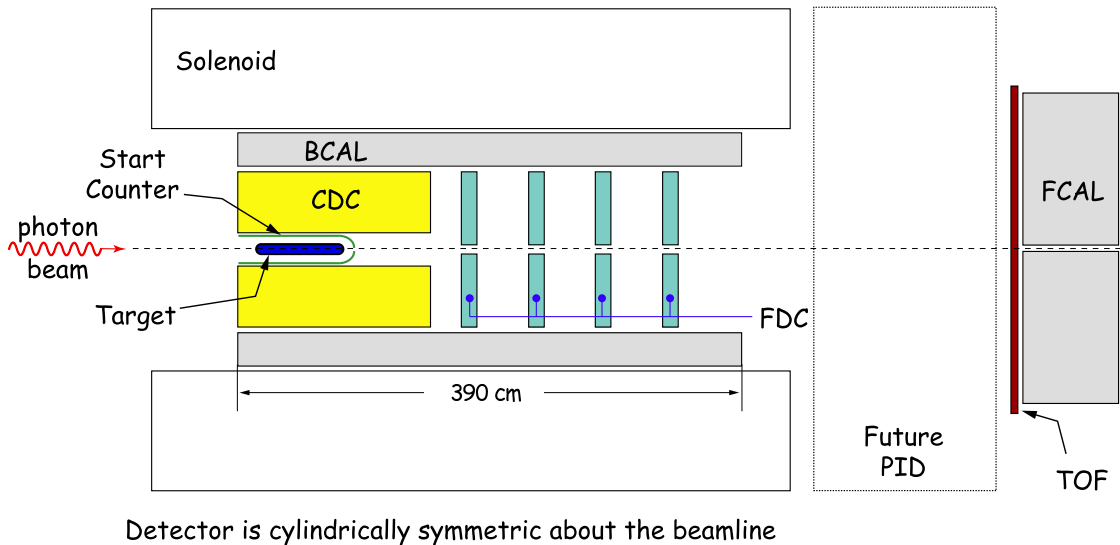


Figure 1: Schematic of the GLUEX detector. A description is provided in the text.

The GLUEX detector uses a geometry based on solenoidal magnetic field, this is ideal for a fixed-target photoproduction experiment (Figure 1). The solenoidal magnetic field traps low energy electromagnetic backgrounds ( $e^+e^-$  pairs) generated in the target inside a cone around the beam. It also allows for effective instrumentation of calorimeters to achieve very high acceptance for photons. The superconducting solenoid produces a 2.25 T field. A tagged,  $\approx 9$  GeV, linearly polarized photon beam is incident on a 30 cm long liquid-hydrogen target that is surrounded by a start counter which is used in triggering. Next is a cylindrical tracking chamber, the CDC, and then a cylindrical electromagnetic calorimeter, the BCAL. Downstream of the CDC are four packages of circular planar drift chambers, FDC, followed by a time-of-flight wall, TOF. This is followed by a circular planar electromagnetic calorimeter, the FCAL. Space has been reserved between the downstream end of the magnet and the TOF for a possible particle identification (PID) system. This design provides for nearly  $4\pi$  acceptance for both charged particles and photons. While the acceptance is not completely uniform in all variables, there are no holes in the kinematic variables of interest.

## 2 Physics motivation: the search for exotic mesons

### 2.1 QCD and light meson spectroscopy

The observation, nearly four decades ago, that mesons are grouped in nonets, each characterized by unique values of  $J^{PC}$  – spin ( $J$ ), parity ( $P$ ) and charge conjugation ( $C$ ) quantum numbers – led to the development of the quark model. Within this picture, mesons are bound states of a quark ( $q$ ) and antiquark ( $\bar{q}$ ). The three light-quark flavors (*up*, *down* and *strange*) suffice to explain the spectroscopy of most – but not all – of the lighter-mass mesons (below  $3 \text{ GeV}/c^2$ ) that do not explicitly carry heavy flavors (charm or beauty). Early observations yielded only those  $J^{PC}$  quantum numbers consistent with a fermion-antifermion bound state. The  $J^{PC}$  quantum numbers of a  $q\bar{q}$  system with total quark spin,  $\vec{S}$ , and relative angular momentum,  $\vec{L}$ , are determined as follows:  $\vec{J} = \vec{L} + \vec{S}$ ,  $P = (-1)^{L+1}$  and  $C = (-1)^{L+S}$ . Thus  $J^{PC}$  quantum numbers such as  $0^{--}$ ,  $0^{+-}$ ,  $1^{-+}$  and  $2^{+-}$  are not allowed and are called *exotic* in this context.

Our understanding of how quarks form mesons has evolved within quantum chromodynamics (QCD) and we now expect a richer spectrum of mesons that takes into account not only the quark degrees of freedom, but also the gluonic degrees of freedom. Gluonic mesons with no quarks (*glueballs*) are expected. These are bound states of pure glue, and since the quantum numbers of low-lying glueballs (below  $4 \text{ GeV}/c^2$ ) are not exotic, they should manifest themselves as extraneous states that cannot be accommodated within  $q\bar{q}$  nonets. But their unambiguous identification is complicated by the fact that they can mix with  $q\bar{q}$ . Excitations of the gluonic field binding the quarks can also give rise to so-called *hybrid* mesons that can be viewed as bound states of a quark, antiquark and valence gluon ( $q\bar{q}g$ ). An alternative picture of hybrid mesons, one supported by lattice QCD [2], is one in which a gluonic flux tube forms between the quark and antiquark and the excitations of this flux tube lead to so-called *hybrid* mesons. Actually the idea of flux tubes, or strings connecting the quarks, originated in the early 1970's [3] to explain the observed linear dependence of the mass-squared of hadrons on spin (Regge trajectories). Conventional  $q\bar{q}$  mesons arise when the flux tube is in its ground state, while hybrid mesons arise when the flux tube is excited. Particularly interesting is that some of these hybrid mesons can have a unique signature, exotic  $J^{PC}$ . The spectroscopy of these exotic hybrid mesons is simplified because they do not mix with conventional  $q\bar{q}$  states.

The level splitting between the ground state flux tube and the first excited transverse modes is  $\pi/r$ , where  $r$  is the separation between the quarks, so the hybrid spectrum should lie about  $1 \text{ GeV}/c^2$  above the ground state spectrum. While the flux-tube model [4] has all hybrid nonets degenerate in mass, from lattice gauge calculations [5], one expects the lightest exotic hybrid (the  $J^{PC} = 1^{-+}$ ) to have a mass of about  $1.9 \text{ GeV}/c^2$ . In this discussion, the motion of the quarks was ignored, but we know from general principles [4] that an approximation that ignores the impact of the flux tube excitation and quark motion on each other seems to work quite well. It should be noted, also, in the large- $N_c$  limit of QCD, exotic hybrids are expected to have narrow widths, comparable to  $q\bar{q}$  states [6]. To be able to map out the spectrum of exotic hybrids, it is important to be able to observe mesons with a mass of  $\approx 2.5 \text{ GeV}/c^2$ , which requires a mass reach up to about  $2.8 \text{ GeV}/c^2$ .

In the coming years there will be significant computational resources dedicated to understanding non-perturbative QCD, including confinement, using lattice techniques. The prediction of the hybrid spectrum, including decays, will be a key part of this program, but experimental data will be needed to verify these calculations. The spectroscopy of exotic mesons provides a clean and attractive starting point for the study of gluonic excitations.

The GLUEX experiment is designed to collect high quality and high statistics data on the photoproduction of light mesons. As part of the program of identifying exotic hybrid mesons, these data will also be used to understand the conventional meson spectrum, including the poorly understood excited vector mesons.

### 2.2 Using linearly polarized photons

There are tantalizing suggestions, mainly from experiments using beams of  $\pi$  mesons, that exotic hybrid mesons exist. The evidence is by no means clear cut, owing in part, to the apparently small production rates for these states in the decay channels examined. It is safe to conclude that the extensive data collected

to date with  $\pi$  probes have not uncovered the hybrid meson spectrum. (A recent paper by E. Klempt and A. Zaitsev gives an encyclopedic and critical overview of the current experimental situation with regard to searches for glueballs, hybrids and multi-quark mesons [7].) Models, like the flux-tube model, however, indicate the photon is a probe that should be particularly effective in producing exotic hybrids.

The first excited transverse modes of the flux tube are degenerate and correspond to clockwise or counter-clockwise rotations of the flux tube around the axis joining the quark and antiquark fixed in space with  $J = 1$  [4]. Linear combinations of these two modes are parity eigenstates and lead to  $J^{PC} = 1^{+-}$  and  $J^{PC} = 1^{-+}$  for the excited flux tube. When these quantum numbers are combined with those of the  $q\bar{q}$  with  $\vec{L} = 0$  and  $\vec{S} = 1$  (quark spins aligned), three of the six possible  $J^{PC}$  have exotic combinations:  $0^{+-}$ ,  $1^{-+}$  and  $2^{+-}$ . A photon probe is a virtual  $q\bar{q}$  with quark spins aligned. In contrast, when the  $q\bar{q}$  have  $\vec{L} = 0$  and  $\vec{S} = 0$  (spins anti-aligned), the resulting quantum numbers of the hybrid meson are not exotic. Pion probes are  $q\bar{q}$  with quark spins anti-aligned. If we view one outcome of the scattering process as exciting the flux tube binding the quarks in the probe, the suppression of exotic hybrids in  $\pi$ -induced reactions is not surprising – a spin flip of one of the quarks is required followed by the excitation of the flux tube. In contrast, the spins of the virtual quarks in the photon probe are properly aligned to lead to exotic hybrids. Phenomenological studies quantitatively support this picture predicting that the photoproduction cross sections for exotic mesons are comparable to those for conventional mesons [8].

Determining the quantum numbers of mesons produced in the GLUEX experiment will require an amplitude analysis based on measuring the energy and momentum of their decay products. Linear polarization of the incident photon is required for a precision amplitude analysis to identify exotic quantum numbers, to understand details of the production mechanism of exotic and conventional mesons and to remove backgrounds due to conventional processes. Linear polarization will be achieved using the coherent bremsstrahlung technique.

For the GLUEX solenoid-based detector system, given the mass reach required (up to  $2.8 \text{ GeV}/c^2$ ) for mapping the spectrum of exotic hybrid mesons, a photon energy of  $\approx 9 \text{ GeV}$  is ideal. The requisite degree of linear polarization for 9 GeV photons can be achieved using coherent bremsstrahlung, but requires a minimum electron energy of 12 GeV.

### 2.3 Expected decay modes of exotic hybrid mesons

Table 1 lists predicted  $J^{PC}$  exotic mesons and their decay modes. According to the flux tube model and verified by lattice QCD [9], the preferred decay modes for exotic hybrids are into  $(q\bar{q})_P + (q\bar{q})_S$  mesons such as  $b_1 \pi$  or  $f_1 \pi$  (the subscripts  $P$  and  $S$  refer to the orbital angular momentum between the quark and antiquark in the meson). Table 2 lists candidate exotic  $J^{PC} = 1^{-+}$  states for which evidence has been claimed. The purported exotic states include decay modes into  $b_1 \pi$  or  $f_1 \pi$ , as well as decay modes into  $\eta \pi$  and  $\eta' \pi$ . The dominant branching fractions for meson states listed among the decay products are summarized in Table 3. Clearly, exotic meson spectroscopy requires the ability to detect and measure charged particles, as well as  $\pi^0$  and  $\eta$  mesons.

Most of the preferred or observed exotic hybrid decay modes listed in Tables 1 and 2 involve several pions. These will occur in final states that only involve  $\pi^\pm$  such as  $(\rho\pi)^+ \rightarrow \pi^+\pi^+\pi^-$ , but also in combinations which include  $\pi^0$ s,  $(\rho\pi)^+ \rightarrow \pi^+\pi^0\pi^0$ . Having all the isospin related final states available provides an extremely important isospin consistency checks of the amplitude analysis and understanding of the detector acceptance.

### 2.4 Information from existing photoproduction data

There is little data on meson photoproduction in the GLUEX energy regime ( $E_\gamma \approx 7 - 9 \text{ GeV}$ ). Almost all of what is known comes from bubble chamber measurements at SLAC [10, 11, 12, 13, 14, 15]. These experiments were among the first exploratory studies of the photoproduction of meson and baryon resonances at these energies, and although they suffer from low-statistics, they have good acceptance, except for events with multiple neutrals. Exclusive reactions leading to final states with charged particles and a single neutron or  $\pi^0$  can be identified by kinematic fitting. Table 4 summarizes the photoproduction cross sections for various

Exotic Meson	$J^{PC}$	$I$	G	Possible Modes
$b_0$	$0^{+-}$	1	+	
$h_0$	$0^{+-}$	0	-	$b_1\pi$
$\pi_1$	$1^{-+}$	1	-	$\rho\pi, b_1\pi$
$\eta_1$	$1^{-+}$	0	+	$a_2\pi$
$b_2$	$2^{+-}$	1	+	$a_2\pi$
$h_2$	$2^{+-}$	0	-	$\rho\pi, b_1\pi$

Table 1: Predicted  $J^{PC}$  exotic hybrid mesons and their expected decay modes. See Table 3 for decay modes of the  $b_1$  and  $a_2$  mesons.

Exotic Meson Candidate	Decay Mode
$\pi_1(1400)$	$\pi^-\eta$ $\pi^0\eta$
$\pi_1(1600)$	$\rho^0\pi^-$ $\eta'\pi^-$
$\pi_1(1600/2000)$	$b_1\pi$ $f_1\pi$

Table 2: Reported  $J^{PC} = 1^{-+}$  exotic hybrid mesons and their decay modes. See Table 3 for decay modes of the  $\eta'$ ,  $b_1$  and  $f_1$  mesons. Source: 2006 Review of Particle Physics [16].

Meson Decay Mode	Branching Fraction (%)
$\pi^0 \rightarrow 2\gamma$	99
$\eta \rightarrow 2\gamma$	39
$\eta \rightarrow 3\pi^0$	33
$\eta \rightarrow \pi^+\pi^-\pi^0$	23
$\omega \rightarrow \pi^+\pi^-\pi^0$	89
$\omega \rightarrow \pi^0\gamma$	9
$\eta' \rightarrow \pi^+\pi^-\eta$	45
$\eta' \rightarrow \pi^0\pi^0\eta$	21
$\eta' \rightarrow 2\gamma$	2
$b_1(1235) \rightarrow \omega\pi$	dominant
$f_1(1285) \rightarrow \pi^0\pi^0\pi^+\pi^-$	22
$f_1(1285) \rightarrow \eta\pi\pi$	52
$a_2(1320) \rightarrow 3\pi$	70
$a_2(1320) \rightarrow \eta\pi$	15

Table 3: Neutral or charged + neutral decay modes of several well established mesons. Source: 2006 Review of Particle Physics [16].

charged particle topologies, with and without neutrals, at  $E_\gamma = 9.3$  GeV [10]. Final states with single or multi-neutral particles ( $\pi^0$ ,  $\eta$  or  $n$ ) account for about 82% of the total cross section. About 13% of the total cross section is due to final states with charged particles and a single  $\pi^0$ . So for about 70% of the total photoproduction cross section, from  $E_\gamma \approx 7$  to  $\approx 12$  GeV, we have essentially no information. Extrapolating from what is known from the final states that have been identified and studied, the bulk of the unknown processes are expected to involve final states with combinations of  $\pi^0$  and  $\eta$  mesons. The discovery potential of GLUEX rests on being able to detect  $\pi^0$  and  $\eta$  mesons in addition to charged particles.

Topology	$\sigma$ ( $\mu\text{b}$ )	% of $\sigma$ with neutrals
1-prong	$8.5 \pm 1.1$	100
3-prong	$64.1 \pm 1.5$	$76 \pm 3$
5-prong	$34.2 \pm 0.9$	$86 \pm 4$
7-prong	$6.8 \pm 0.3$	$86 \pm 6$
9-prong	$0.61 \pm 0.08$	$87 \pm 21$
With visible strange decay	$9.8 \pm 0.4$	-
Total	$124.0 \pm 2.5$	$82 \pm 4$

Table 4: Topological photoproduction cross sections for  $\gamma p$  interactions at 9.3 GeV from Reference [10]. Also shown are the percent of the cross section with neutral particles for each topology.

## 2.5 Studies using PYTHIA

As noted above, much is unknown about photoproduction at GLUEX energies leading to multi-neutral final states. To estimate photon yields, we used the Monte Carlo program PYTHIA [17] that was written to generate high-energy physics events produced in a wide variety of initial states, including fixed target photoproduction. The program is based on a combination of analytical results and QCD-based models of particle interactions. PYTHIA was designed to allow for tuning parameters to suit the particular situation – for example, photoproduction at 9 GeV. The output of the simulations was compared [18] to published data, in particular, reference [10]. Comparison of cross section estimates for charged particle topologies and several reactions in the 3-prong and 5-prong final states, which account for 80% of the total cross section, are shown in Tables 5 and 6. The vector mesons  $\rho$ ,  $\omega$  and  $\phi$  appear in the 3-prong sample in the  $\pi^+\pi^-p$ ,  $\pi^+\pi^-\pi^0p$  and  $K^+K^-p$  final states, respectively. The distribution in  $|t|$  for PYTHIA events agrees with published data for specific reactions. PYTHIA also accounts for  $\Delta$  resonance production. In the  $\pi^+\pi^-K^+K^-p$  state, the  $K^*(890)$  is present in PYTHIA.

Topology	PYTHIA Estimates ( $\mu\text{b}$ )	Data ( $\mu\text{b}$ )
1-prong	$8.8 \pm 0.02$	$8.5 \pm 1.1$
3-prong	$63.5 \pm 0.09$	$64.1 \pm 1.5$
5-prong	$42.7 \pm 0.2$	$34.2 \pm 0.9$
7-prong	$7.3 \pm 0.1$	$6.8 \pm 0.3$
9-prong	$0.3 \pm 0.1$	$0.61 \pm 0.08$

Table 5: Topological photoproduction cross sections at 9 GeV from PYTHIA and from bubble chamber data [10]. The PYTHIA cross section estimates have been normalized to a total photoproduction cross section of 124  $\mu\text{b}$ . The errors on the PYTHIA estimates are statistical.

Photoproduction of meson resonances in the GLUEX energy regime typically result in the meson being produced at small absolute values of the momentum transfer squared  $|t|$  between the incoming photon and the outgoing meson – or equivalently between the target proton and the recoil nucleon or baryon resonance. The produced meson, as well as its decay products (depending on the particle multiplicity and relative mother-daughter masses), move in the forward direction, whereas the recoil baryon moves at large angles

Reaction	PYTHIA Estimates ( $\mu\text{b}$ )	Data ( $\mu\text{b}$ )
$\gamma p \rightarrow 3$ prongs		
$\gamma p \rightarrow p\pi^+\pi^-$	$13.6 \pm 0.13$	$14.7 \pm 0.6$
$\gamma p \rightarrow pK^+K^-$	$0.41 \pm 0.02$	$0.58 \pm 0.05$
$\gamma p \rightarrow p\bar{p}p$	$0.04 \pm 0.01$	$0.09 \pm 0.02$
$\gamma p \rightarrow p\pi^+\pi^-\pi^0$	$5.8 \pm 0.1$	$7.5 \pm 0.8$
$\gamma p \rightarrow n2\pi^+\pi^-$	$1.4 \pm 0.04$	$3.2 \pm 0.7$
With multi-neutrals	$42.3 \pm 0.3$	$38.0 \pm 1.9$
$\gamma p \rightarrow 5$ prongs		
$\gamma p \rightarrow p2\pi^+2\pi^-$	$2.9 \pm 0.06$	$4.1 \pm 0.2$
$\gamma p \rightarrow pK^+K^-\pi^+\pi^-$	$0.51 \pm 0.03$	$0.46 \pm 0.08$
$\gamma p \rightarrow p2\pi^+2\pi^-\pi^0$	$8.12 \pm 0.1$	$6.7 \pm 1.0$
$\gamma p \rightarrow n3\pi^+2\pi^-$	$0.8 \pm .3$	$1.8 \pm 1.9$
With multi-neutrals	$30.4 \pm 0.2$	$21.1 \pm 1.7$

Table 6: Photoproduction reaction cross sections at 9 GeV from PYTHIA and from bubble chamber data [10]. The PYTHIA cross section estimates have been normalized to a total photoproduction cross section of  $124 \mu\text{b}$ . The errors on the PYTHIA estimates are statistical.

$\gtrsim 45^\circ$  with respect to the beam direction. If the recoil baryon is a resonance, such as a  $\Delta$  or  $N^*$ , decays involving pions will occur. These baryon-resonance reactions are also expected to be a fruitful place to search for exotic hybrids. GLUEX will be able to exclusively identify these final states, by detecting the soft, wide-angle pion from the resonance decay.

Photoproduction of mesons using a  $\approx 9$  GeV, linearly polarized photon beam provides a unique opportunity to search for exotic hybrids. Existing data is extremely limited for charged final states, and no data exist for multi-neutral final states. To carry out such a search, GLUEX will need to look at many different final states involving both charged particles and photons, but particular emphasis will be placed on those reactions that have 3 or more pions in the final state. The discovery potential for GLUEX comes first from the very high statistics (at least  $10^7$  tagged photons per second on target), which will exceed existing photoproduction data by 4 to 5 orders of magnitude, (and even the best spectroscopy experiments to date by 1 to 2 orders of magnitude). Second, GLUEX has the ability to study many different final states in the same detector. These two effects will not only identify hybrids if they exist, but also map out their decay properties.



### 3 Physics Analysis in GlueX

The ultimate goal of the GLUEX experiment is to identify exotic mesons by an amplitude analysis of exclusive final states. The sensitivity of the amplitude analysis, *i.e.* how small a signal can be detected, depends on having sufficient statistics and how well systematics, both from the experiment and from the analysis, are controlled. GLUEX collaborators have recently been awarded an NSF grant to develop tools for understanding the phenomenological systematics inherent in an amplitude analysis. To estimate the sensitivity we expect from GLUEX requires a full simulation of the detector response to real and background events, charged particle and photon reconstruction, kinematic fitting to identify exclusive final states and finally the actual amplitude analysis. Work is in progress on all of these, but the complete study has not yet been completed. In the following, we perform a comparison of what has been done in a successful spectroscopy experiment (Brookhaven E852) and what is expected in GLUEX.

The E852 experiment used an 18 GeV/c  $\pi^-$  beam incident on a hydrogen target. The detector is a spectrometer based on a dipole magnet that produced nearly-uniform 1 T magnetic field over a volume that was 1.8 m wide (in the bend plane), 1.2 m high and 4.6 m long (along the beam line). E852 also had a calorimeter downstream of the dipole for detecting photons. GLUEX has about one-half the beam energy as E852, and uses a 4 m long, 2.25 T solenoidal field for tracking charged particles. GLUEX has both a downstream calorimeter and a second calorimeter in the barrel region. While E852 has very good momentum resolution for forward-going charged particles, it was unable to reconstruct recoil protons from the target. GLUEX has reduced tracking resolutions for the forward going particles, but better acceptance for recoil protons. GLUEX also has a larger calorimeter coverage than E852. While a system-by-system comparison of the two detectors is interesting, the true measure of their abilities comes from reconstructed spectra that are related to the underlying physics. In the following, we present these comparisons (as taken from reference [19]).

#### 3.1 A signature reaction: $\gamma p \rightarrow 3\pi p$

Recently a high-statistics study of the reactions

$$\begin{aligned}\pi^- p &\rightarrow p\pi^+\pi^-\pi^- \\ \pi^- p &\rightarrow p\pi^-\pi^0\pi^0\end{aligned}$$

was performed using data from E852 [20]. The corresponding reaction of interest in GLUEX is

$$\gamma p \rightarrow n\pi^+\pi^+\pi^-.$$

Using the underlying physics observed in E852, Monte Carlo events were generated for GLUEX. Equal numbers of events corresponding to  $\gamma p \rightarrow a_2^+(1320)n$  and  $\gamma p \rightarrow \pi_2^+(1670)n$  were generated followed by the decays  $a_2 \rightarrow \rho\pi \rightarrow 2\pi^+\pi^-$  and  $\pi_2 \rightarrow f_2\pi \rightarrow 2\pi^+\pi^-$ . This approximates the mass distributions observed in the E852 experiment for  $\pi^- p \rightarrow 2\pi^-\pi^+p$  at an incident momentum of 18 GeV/c. For the Monte Carlo sample we assume a photon beam energy of 9 GeV. The  $|t|$  distribution followed a form  $e^{-5\cdot|t|}$  and all the resonances have uniform angular decay distributions. In the E852 study of this reaction [20], the presence of a proton charged track is required in the trigger, but the momentum of the proton is not measured. The distributions in  $|t|$ , the  $3\pi$  mass, the like-sign  $2\pi$  mass and  $\pi^+\pi^-$  mass for our Monte Carlo sample and for acceptance-uncorrected E852 data are shown in Figure 2. For the GLUEX events, the momenta and angles of the generated events were smeared according to parameterized resolution functions<sup>1</sup> [21]. The distributions for both GLUEX and E852 are quite comparable.

For both the GLUEX simulation and the E852 data, information about the nucleon recoiling against the  $3\pi$  system is not used in kinematically identifying the event. Thus, a comparison of the missing mass is of

<sup>1</sup>The parameterizations were based on resolution studies carried out using a detector model from 2007. It does not include the reduction of material in the FDC and CDC and the other design changes that have occurred since then. However, studies show that this is a good approximation to what would be expected using the current resolutions.

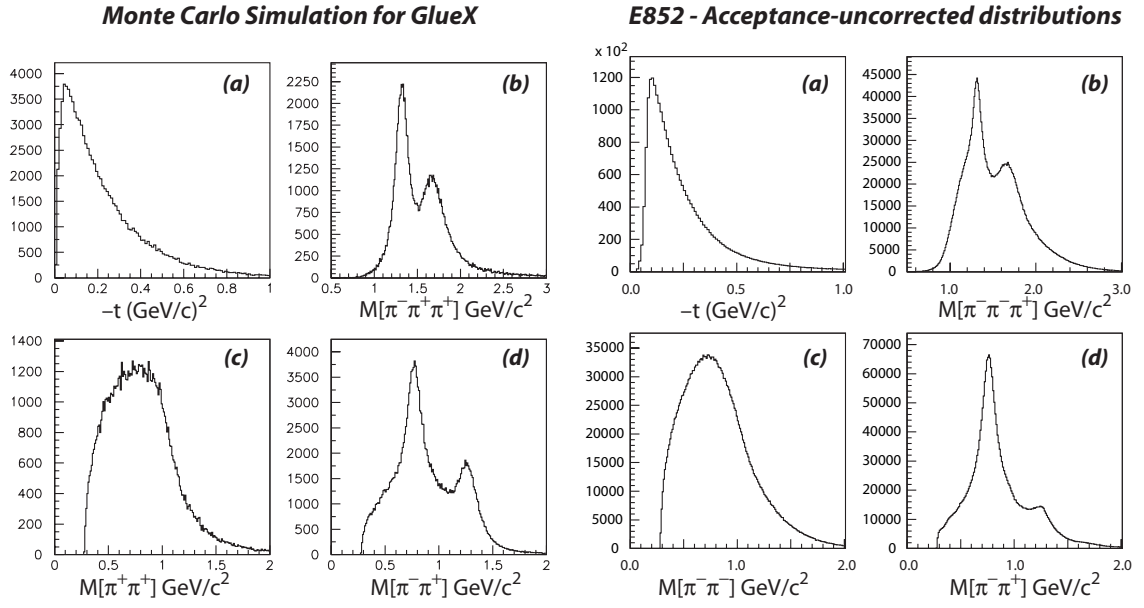


Figure 2: Physics distributions for the  $3\pi$  final state. The left-hand plots are for simulated GLUEX  $\pi^+\pi^+\pi^-$  data while the right-hand plots are for E852 [20]  $\pi^-\pi^-\pi^+$  data (plot taken from reference [19]).

interest. The missing mass squared distribution for the GLUEX Monte Carlo sample is shown in Figure 3 along with a Gaussian fit (solid line). The  $\sigma$  for the Gaussian fit is  $0.27 (\text{GeV}/c^2)^2$ . The corresponding E852 missing mass squared distribution had a  $\sigma$  of  $0.31 (\text{GeV}/c^2)^2$ .

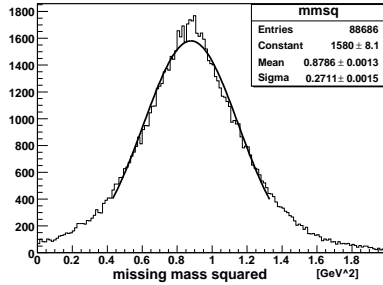


Figure 3: Distribution in missing mass squared recoiling against the  $3\pi$  system for the Monte Carlo sample after resolution smearing. The distribution is centered at  $m_n^2$  and the  $\sigma$  for the Gaussian fit (solid curve) is  $0.27 (\text{GeV}/c^2)^2$ . The corresponding E852 missing mass squared distribution had a  $\sigma$  of  $0.31 (\text{GeV}/c^2)^2$  (plot taken from reference [19]).

How do GLUEX and E852 compare? The resolutions obtained for the  $\pi^0$  mass resolutions for GLUEX calorimetry are similar to those obtained in E852. Studies have been done to estimate the charged particle momentum and angle resolutions. The  $\pi^-\pi^-\pi^+$  and  $\pi^-\pi^+$  effective mass distributions and the distribution in the momentum transfer from the incoming beam to the outgoing  $3\pi$  system observed in E852 were used to generate a Monte Carlo event sample of a similar final state for 9 GeV photoproduction. Charged particle momenta and angles were smeared using current best-estimate resolution functions and the result was that the resolution in the square of the missing-mass recoiling against the  $3\pi$  system for GLUEX will be at least as good as that in E852. This would indicate that the ability to kinematically identify exclusive reactions

should also be at least as good.

### 3.2 Expectations for amplitude analysis

With the previous comparison, we can turn to results of analysis from experiment E852 at Brookhaven. Data were collected from  $\pi^-p$  interactions at 18 GeV/c leading to the final states  $\pi^-\pi^0\pi^0p$  and  $\pi^-\pi^-\pi^+p$  [20]. That experiment used the multiparticle spectrometer (MPS) at the AGS. Figure 4 shows the results of an amplitude analysis for the  $J^{PC} = 2^{++}$  and  $J^{PC} = 4^{++}\rho\pi$  amplitudes. Two well-established meson states are observed in these amplitudes, the tensor state  $a_2(1320)$  in the former and the spin-4 state  $a_4(2040)$  in the latter. The intensity of the  $a_4$  is about 3% that of the  $a_2$  and the amplitude of the  $a_4$  is similar for the  $\pi^-\pi^0\pi^0$  and  $\pi^-\pi^-\pi^+$  systems, even though the experimental systematics for these two modes are very different.

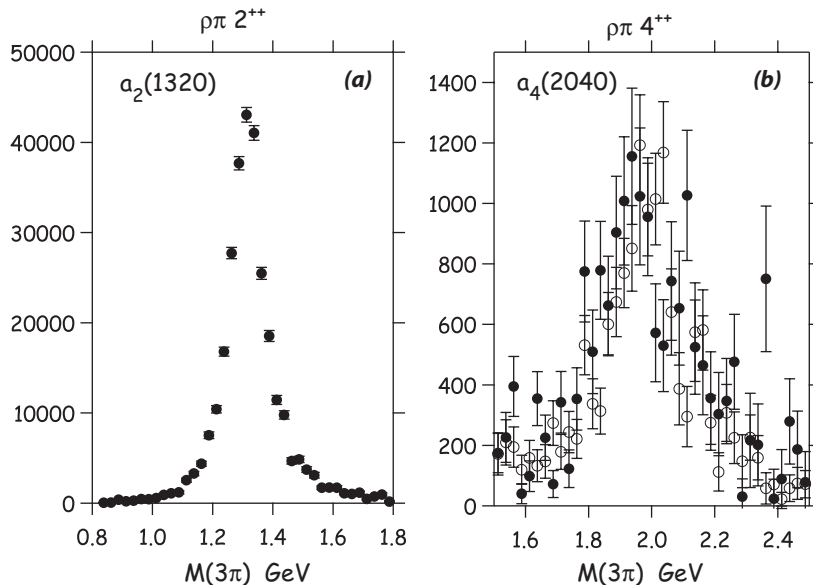


Figure 4: (a) Results of an amplitude analysis of data from  $\pi^-p$  interactions at 18 GeV/c leading to the final states  $\pi^-\pi^0\pi^0p$  and  $\pi^-\pi^-\pi^+p$  from Brookhaven experiment E852 [20]. Results are shown for the (a)  $J^{PC} = 2^{++}$  and (b)  $J^{PC} = 4^{++}\rho\pi$  amplitudes. Filled circles are for the  $\pi^-\pi^0\pi^0$  system and unfilled for the  $\pi^-\pi^-\pi^+$  system. In (a) the tensor state  $a_2(1320)$  is observed and in (b) the well-established spin-4  $a_4(2040)$  is seen. Note that the intensity of the  $a_4$  is about 3% that of the  $a_2$ .

Given the success of E852 in extracting a small signal, we expect that GLUEX should be able to reach the same level of sensitivity. In photoproduction, the  $a_2$  production cross section is about  $0.5 \mu\text{b}$ , for a similar statistics data set to E852, a 15 nb cross section should be observable in GLUEX and with the expected higher statistics, this lower limit could be even smaller.

### 3.3 Other mass distributions

#### 3.3.1 $K_S^0$ events

Another signature GLUEX reaction which has been studied [22] is:

$$\gamma p \rightarrow K^{*+}(890)K^{*-}(890)p \rightarrow K_S^0\pi^+K_S^0\pi^-p$$

where  $K_S^0 \rightarrow \pi^+\pi^-$  so the final state has  $3\pi^+3\pi^-$ . The  $K^{*+}(890)K^{*-}(890)$  are decay products of  $X$  whose mass is chosen uniformly between 2.0 and 2.5 GeV/ $c^2$  and is produced with a  $|t|$  dependence  $\propto e^{-5\cdot|t|}$ . The

$K\pi K\pi p$  resulting from  $K^{*+}(890)K^{*-}(890)p$  is kinematically similar to other intermediate states leading to  $K\pi K\pi p$  and to what is generated by PYTHIA. This channel has important discovery potential for exotic  $s\bar{s}$  hybrids.

The momentum and lab angle spectra and their correlation for the  $K_S^0$  are shown in Figure 5. The momenta and angles of all charged tracks were smeared to follow the estimates of the resolution in momentum ( $p$ ), polar angle ( $\theta$ ) and azimuthal angle ( $\phi$ ) as functions of these variables. Figure 5(d) shows the distribution in all  $\pi^+\pi^-$  effective mass combinations for nominal resolutions (solid) and for the case when the momentum resolution is degraded by a factor of two.

As a check of uniformity, the correlation plot of Figure 5(a) is divided into four regions, of roughly equal population, as shown where the dividing lines are at a momentum of 2.5 GeV and at an angle of  $10^\circ$ . Table 7 shows the  $K_S^0$  mass resolution for these regions under two assumptions about the momentum resolution.

Region	Nominal Resolution	Degraded Resolution
I	$7.4 \pm 0.2$ MeV	$13.8 \pm 0.3$ MeV
II	$9.4 \pm 0.2$ MeV	$16.6 \pm 0.3$ MeV
III	$7.2 \pm 0.2$ MeV	$13.2 \pm 0.3$ MeV
IV	$5.9 \pm 0.2$ MeV	$10.8 \pm 0.3$ MeV

Table 7:  $K_S^0$  mass resolutions assuming nominal tracking resolution and for the momentum resolution degraded by a factor of two (resolutions come from [21]). The regions refer to those in Figure 5(a) (table taken from reference [22]).

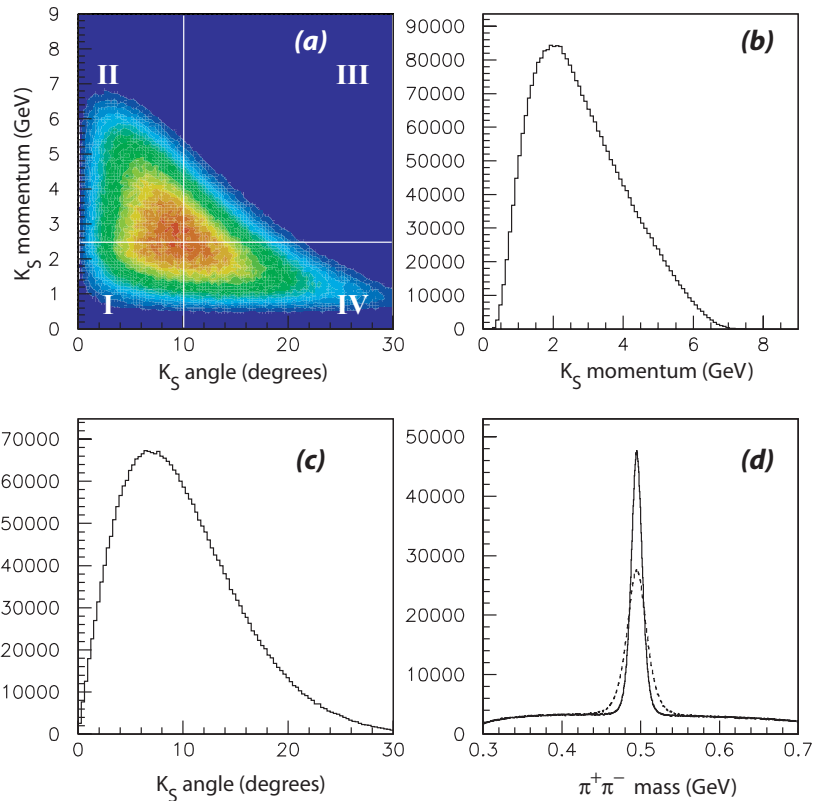


Figure 5: Kinematics of the  $K_S^0$  for the reaction  $\gamma p \rightarrow K_S^0 \pi^+ K_S^0 \pi^- p$ . Please see text for details (figure taken from reference [22]).

The nominal mass resolutions for a narrow state like the  $K_S$  are very good and reasonably uniform over the detector acceptance.

### 3.3.2 Mass resolutions involving charged particles and photons

Many of the expected decay modes of exotic hybrids involve narrow daughter products such as  $\eta$ ,  $\omega$  and  $\phi$ . To compare the contributions of charged particle resolution and photon resolutions to narrow width particles, as in the decays  $\eta \rightarrow \pi^+\pi^-\pi^0$ ,  $\omega \rightarrow \pi^+\pi^-\pi^0$  and  $\phi \rightarrow \pi^+\pi^-\pi^0$ , we studied the reaction  $\gamma p \rightarrow \phi p$  [1]. For this study, the distribution in  $|t|$  followed  $e^{-|t|/2}$  to provide a mix of charged particle momenta that would include more lower momentum particles. The  $\phi$  was generated with a mass and width of 1020 and 4 MeV/ $c^2$  respectively. The charged particle four vectors (for the  $\pi^\pm$ ) were smeared to follow the momentum error and angular error plots generated in a study of track finding in GLUEX [21]. The plots shown in the referenced study were fit to analytical forms. These plots were generated before the material associated with the CDC and FDC tracking chambers was reduced so the nominal charged particle resolutions are somewhat over estimated. The study also considered what would happen if the nominal charged particle resolutions improved by a factor of two. The effect of the resolution smearing on the observed width of the  $\phi$  is shown in Table 8. The distribution in the square of the missing mass recoiling against the  $\phi$  is shown in Figure 6 under the same assumptions of four-vector smearing. The nominal errors associated with the charged particles are very similar to those for the  $\pi^0$  in both of these cases.

Condition	Nominal errors for $\pi^\pm$	Nominal errors/2 for $\pi^\pm$
Photon smearing only	$14.8 \pm 0.1$ MeV/ $c^2$	$14.8 \pm 0.1$ MeV/ $c^2$
Charged particle smearing only	$16.7 \pm 0.1$ MeV/ $c^2$	$11.1 \pm 0.1$ MeV/ $c^2$
Both smeared	$22.2 \pm 0.2$ MeV/ $c^2$	$17.6 \pm 0.1$ MeV/ $c^2$

Table 8: Observed width for the  $\phi$ , generated with a width of 4 MeV/ $c^2$ , after four-vector smearing.

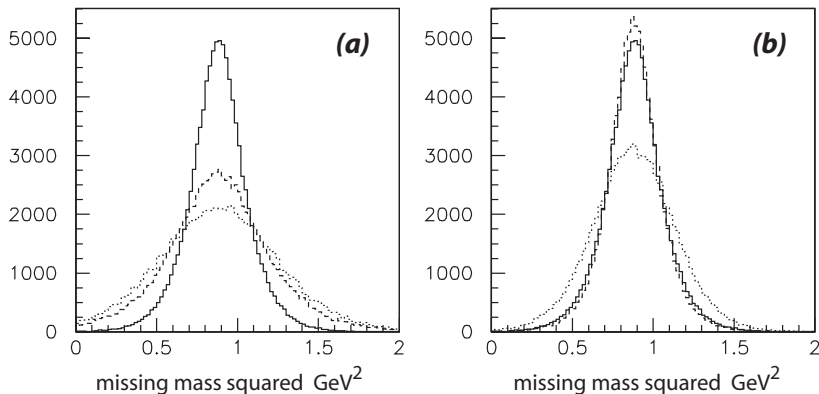


Figure 6: Missing mass squared recoiling off the  $\phi$  for the reaction  $\gamma p \rightarrow \phi p$  with photon smearing only (solid histogram), charged particle smearing only (dashed) and both (light dashed) for nominal charged particle smearing (a) and smearing reduced by a factor of two (b) (figure taken from reference [1]).

### 3.4 Kinematic fitting of exclusive final states

GLUEX will measure exclusive final states in order to carry out amplitude analysis. This means that physics constraints such as energy and momentum conservation, as well as the masses of particles that decay to photons can be used to constrain and improve the measurements of particle momentum and energy. The technique for doing this is known as kinematic fitting [23]. In order to show the effects of kinematic fitting in

GLUEX, we have examined reactions involving  $\omega$  mesons decaying to  $\pi^+\pi^-\pi^0$ . For simple photoproduction of the  $\omega$  meson, we have

$$\gamma p \rightarrow p\omega \rightarrow p\pi^+\pi^-\pi^0.$$

In this reaction, we assume that the  $\pi^0$  is completely missing. The  $\pi^0$  four-momentum is initially computed via energy and momentum conservation, and then the invariant mass of the three pion system is computed. This is shown in the left-hand plot in Figure 7, where we observe a mass resolution of about  $0.32 \text{ GeV}/c^2$ . Next, we perform a 1-constraint fit to the hypothesis of a missing  $\pi^0$ . The right-hand plot of Figure 7 shows the resulting invariant mass after the fit. In this particular situation, the fit has improved the mass resolution by a factor of two.

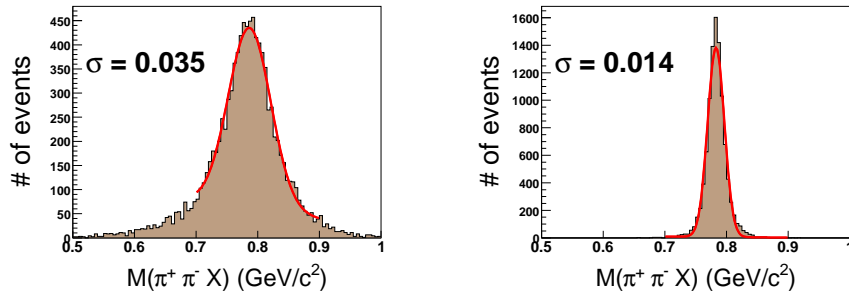


Figure 7: The reaction  $\gamma p \rightarrow p\omega$ . (left) is the  $3\pi$  invariant mass before kinematic fitting, (right) is the same distribution after a 1-constraint fit to a missing  $\pi^0$  is performed (See text for details.).

In a related reaction, we consider

$$\gamma p \rightarrow p\pi^+\pi^-\omega \rightarrow p\pi^+\pi^-\pi^+\pi^-\pi^0.$$

Here, the additional pions produce a combinatorial background that makes it more difficult to identify the  $\omega$ . Performing the same analysis, treating the  $\pi^0$  as missing, and then computing all the neutral three-pion mass combinations, we go from the prefit distribution shown on the left of Figure 8 to the fit distribution on the right. Again, we see the resolution improving by about a factor of two with a significant reduction in the combinatorial backgrounds.

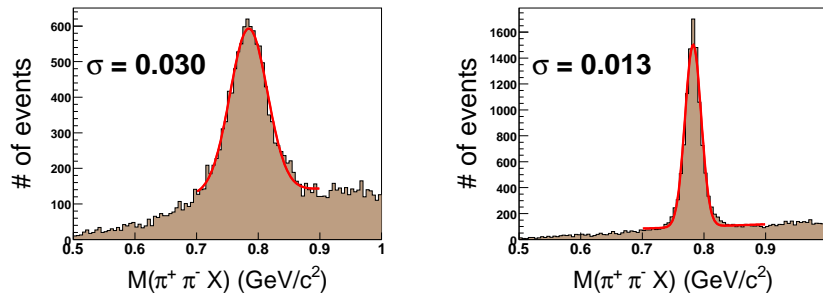


Figure 8: The reaction  $\gamma p \rightarrow p\pi^+\pi^-\omega$ . (left) is the  $3\pi$  invariant mass before kinematic fitting, (right) is the same distribution after a 1-constraint fit to a missing  $\pi^0$  is performed (see text for details.).

The one-constraint fits shown here are examples of the least constrained fitting that can be done in GLUEX. In the same reaction, with the  $\pi^0$  measured and the nucleon missing, we have a second constraint,

the mass of the  $\pi^0$ . In the case where all particles are detected, the fit would have five constraints. As the number of constraints goes up, the ability to separate reactions with kinematic fitting improves. As with most other spectroscopy experiments, kinematic fitting will be an important analysis tool for GLUEX.

## 4 Reconstruction of charged particles in GlueX

Charged particles ( $\pi^\pm$ ,  $K^\pm$  and  $p$ ) will be reconstructed using two tracking systems. The CDC around the target and the FDC in the downstream half of magnet. The CDC [24] is a 24-layer, 1.5-m long straw tube chamber, while the FDC [25] packages are cathode-plane drift chambers. These are described in detail in the references. Here we only note that the CDC should achieve a  $150\ \mu\text{m}$  resolution normal to the wire. Using stereo layers, a  $z$  resolution along the wire of about  $\sim 1.5\ \text{mm}$  can be achieved. The FDC will make measurements in the  $x$ - $y$  plane (normal to the beam direction) with a resolution of  $200\ \mu\text{m}$ . Together, these detectors will track particles from threshold up to nearly  $8\ \text{GeV}/c$ . The kinematics of the photoproduction reaction tend to give the particles a forward boost with the highest momentum particles traveling at small angles and essentially being only detected in the FDC. Particles with larger transverse momentum tend to have lower overall momentum and will be tracked in some combination of the two chambers.

The angular regions of detection can roughly be divided as follows. Particles going more forward than about  $1^\circ$  in the lab will go down the beamline and not be detected by any tracking detector. Outside of this, to about  $6^\circ$ , particles will be tracked only in the FDC. From  $6^\circ$  out to  $30^\circ$ , particles can be detected by both the CDC and the FDC. Realistically, for both the CDC and the FDC to be used in reconstruction, the particles are in the range of about  $8^\circ$  to  $24^\circ$ . From  $30^\circ$  to about  $150^\circ$ , particles will be reconstructed in the CDC alone. In fact, hits will be observed in the CDC back to  $168^\circ$ , but the track resolution will be reduced due to the fact that the number of hits along a track will be fewer than 10. However, for the key physics program in GLUEX, there will be essentially no particles at such large angles.

### 4.1 Momentum resolution

As discussed above, charged particles are reconstructed in the detector using the CDC and FDC. To determine the momentum resolution for charged particles in GLUEX, the particles are tracked using the detector simulation package HDGEANT [26],[27] based on GEANT 3.14. This simulation contains our best estimate of all the material in GLUEX, as well as models for all relevant detector responses. The resulting events are then reconstructed using the GLUEX reconstruction software [21, 28]. The current software uses hits from the chambers with design resolutions to find, and then fit the tracks. Both the Monte Carlo and the reconstruction software use a realistic field map for the solenoidal magnetic field including fringe fields that extend out to the time-of-flight wall. The fit momentum is then compared with the generated momentum, which yields to the resolution plots shown in this section.

We start with the momentum resolution,

$$\sigma_{\Delta p/p} = \frac{\Delta |\vec{p}|}{|\vec{p}|}.$$

Figure 9 shows a plot of momentum resolution versus polar angle for several fixed values of total momentum in the range of 1 to 7 GeV/c. There are several structures seen in Figure 9 that can be understood in terms of the geometry of the detector. The degradation in resolution for very forward tracks is due to the small bending for these tracks, which go roughly parallel to the magnetic field in GLUEX. The degradation that occurs in the angular range of  $10^\circ$  to  $25^\circ$  correspond to particles not hitting all the FDC packages (a jump is observed each time a package is not hit). The rise in the backwards direction corresponds to particles passing through the upstream endplate of the CDC—however this structure is in a region of phase space that has no events. In fact, most of the angular region backwards of  $40^\circ$  will rarely have particles of momentum larger than  $2\ \text{GeV}/c$ . Most particles in this region will have a momentum resolution better than 1.5%.

We next look at the polar angle resolution,

$$\sigma_{\Delta\theta} = \Delta\theta.$$

Figure 10 shows the angular resolution for slices of polar angle  $\theta$  going from  $10^\circ$  to  $90^\circ$ . Finally, the azimuthal angular resolution

$$\sigma_{\Delta\phi} = \Delta\phi$$



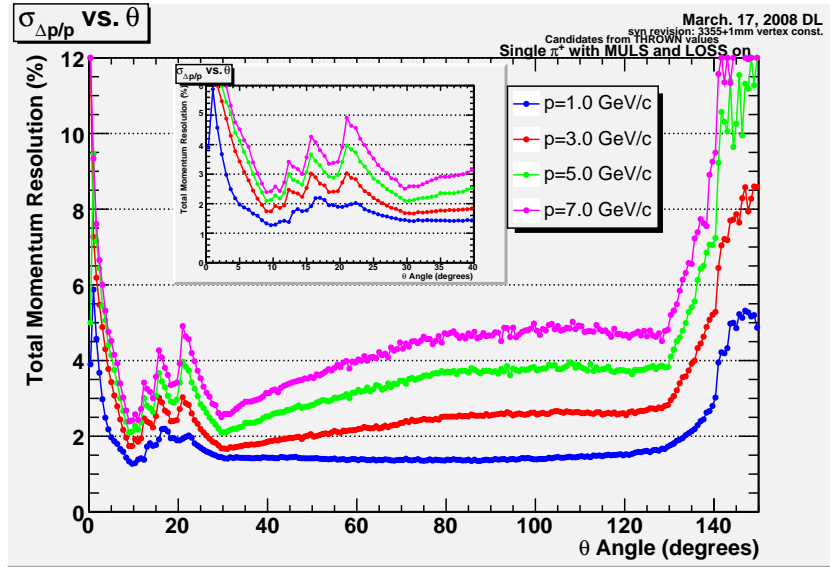


Figure 9: Momentum resolution (%) as a function of the polar angle  $\theta$  at the primary vertex for several values of momentum  $p$  (figure taken from reference [28]).

is shown in Figure 11.

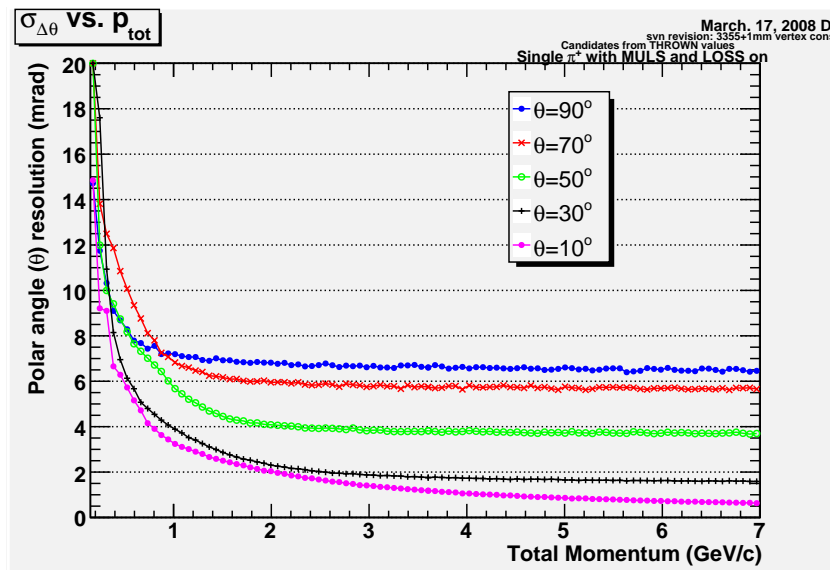


Figure 10: Polar angle resolution (mrad) as a function of the total momentum  $p$  for various polar angle  $\theta$  at the primary vertex (figure taken from reference [28]).

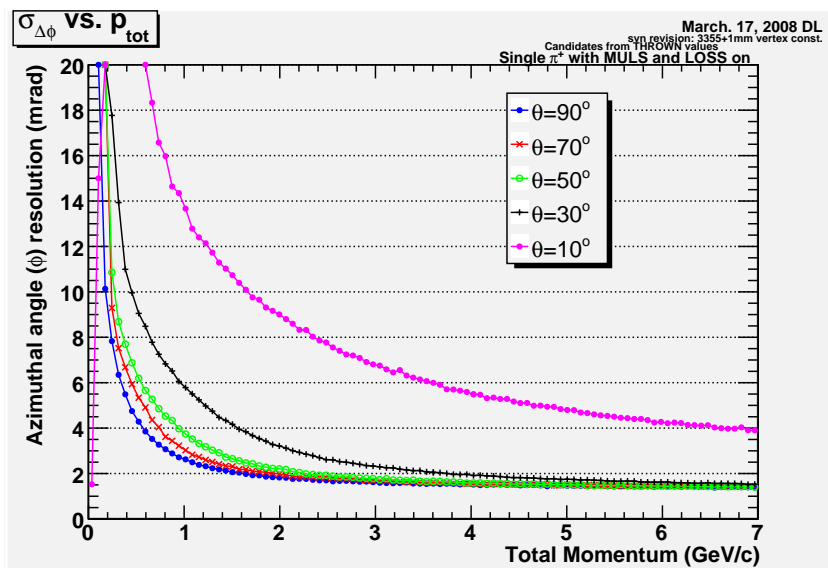


Figure 11: Polar angle resolution (mrad) as a function of the total momentum  $p$  for various polar angle  $\theta$  at the primary vertex (figure taken from reference [28]).

## 4.2 Track finding and fitting

The current version of the GLUEX reconstruction software starts with a track-finding package that looks for tracks in the CDC and FDC separately, and then tries to merge them. Figure 12 shows the track-finding efficiency for this package as a function of both total number of hits and which chambers the tracks are located. The solid triangles show the track finding efficiency as a function of the polar angle  $\theta$  when only the FDC is used. The solid squares show the same plot for the CDC. The solid circles show the efficiency for finding either a CDC or FDC track. The colored regions labeled FDC and CDC map the number of hits on the track in the particular detector. Overall, there is good track-finding efficiency in GLUEX with nearly 100% efficiency everywhere. wTrack-finding in the presence of electromagnetic backgrounds have also been studied in GLUEX. These studies show a few percent, degradation of the efficiencies shown here [28].

After carrying out track finding, the tracks need to be fit to obtain particle information. A track fitting package has been developed, but as with track finding, developmental improvements will continue over the next five years. At present, the GLUEX track fitter is not quite as efficient as track finding. The current losses appears to be related to pathologies in the fitting routines. Work on resolving these deficiencies is in progress, and it is anticipate that the GLUEX track fitting efficiency will improve to more closely match that of track finding [28].

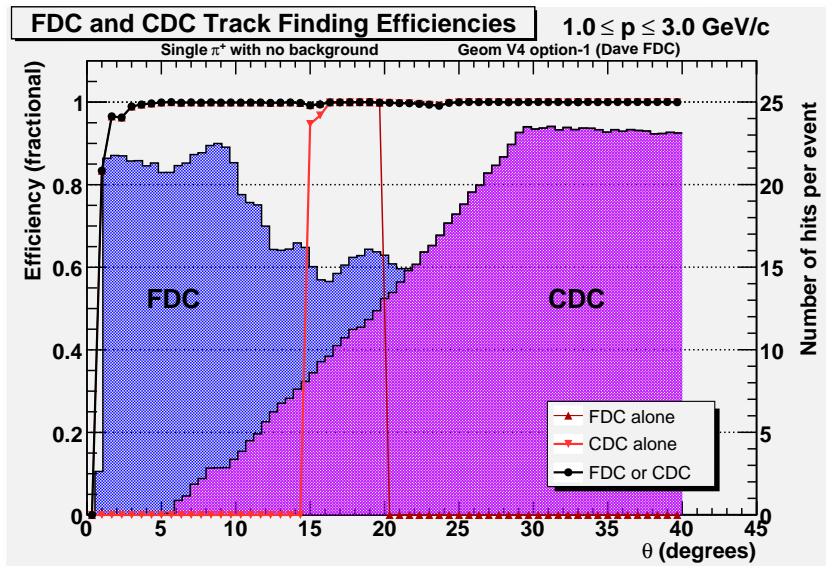


Figure 12: Track finding efficiency in the CDC and FDC, see text for explanation (figure taken from reference [28]).

Based on the resolutions obtained from HDGEANT and the GLUEX reconstruction software, a set of parameterized resolution and acceptance functions have been developed. These functions provide a pseudo event reconstruction which can be used to carry out more sophisticated GLUEX studies. An example of these studies are studies of effective and missing mass resolutions earlier in this report.

## 4.3 Kinematics for reactions of interest in GlueX

In order to understand how particles of various momenta populate the tracking elements, we need to consider some typical reactions that are part of the GLUEX physics program [31]. The first of these is the generic reaction  $\gamma p \rightarrow pX$ , where  $X$  represents a mesonic system with mass less than  $2.5 \text{ GeV}/c^2$ . Such a reaction is expected to be produced in a  $t$ -channel process where the cross section has an exponential dependence on the magnitude of  $t$ ,  $e^{-\alpha|t|}$ , with the slope,  $\alpha$  varying from 2 to 5. Such a reaction defines the proton kinematics in the GLUEX detector. Figure 13 shows the lab momentum and angles for protons produced in the reaction

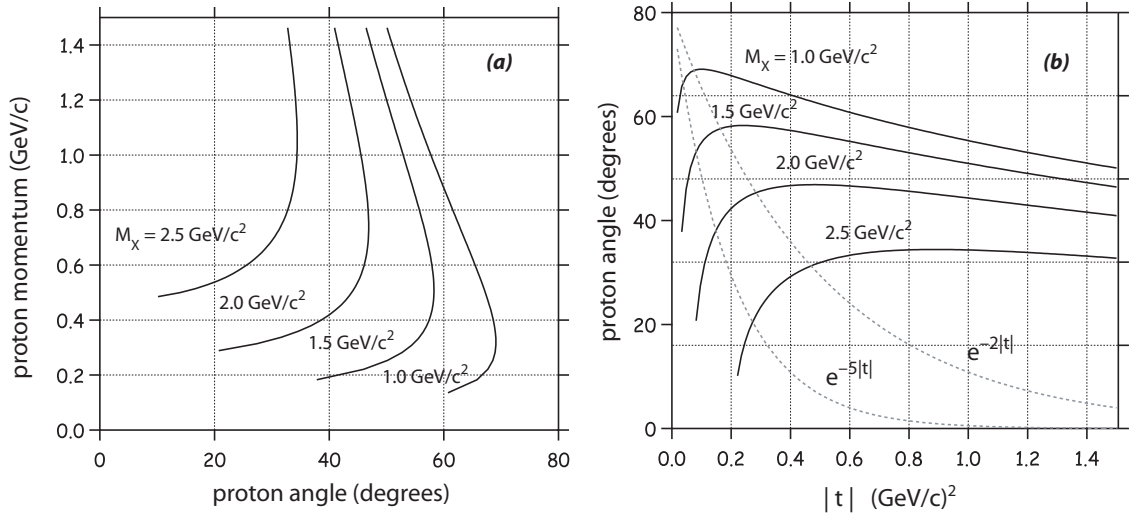


Figure 13: (a) Recoil proton LAB momentum as a function of proton LAB angle, measured with respect to the beam direction, for  $|t|_{min} < 1.5 \text{ (GeV}/c)^2$  for the reaction  $\gamma p \rightarrow Xp$  for  $M_X = 1.0, 1.5, 2.0$  and  $2.5 \text{ GeV}/c^2$ . (b) Recoil proton LAB angle, measured with respect to the beam direction as a function of  $|t|$  for the reaction  $\gamma p \rightarrow Xp$  for  $M_X = 1.0, 1.5, 2.0$  and  $2.5 \text{ GeV}/c^2$ . Also shown are typical  $t$  distributions for  $e^{-2|t|}$  and  $e^{-5|t|}$  (light dotted curves) (figure taken from reference [31]).

$\gamma p \rightarrow pX$  with  $X$  varying in mass from  $1.0$  to  $2.5 \text{ GeV}/c^2$ . Virtually all of these protons are detected in the forward half of the CDC, with many of them also tracked into the FDC packages. For  $m_X = 2.5 \text{ GeV}/c^2$ , the most forward protons have a total momentum of about  $0.4 \text{ GeV}/c$  with this momentum becoming smaller as the mass of  $X$  gets smaller.

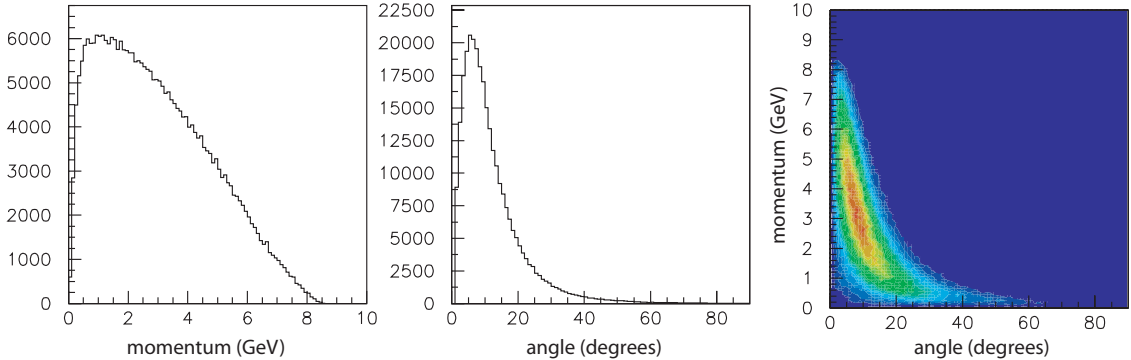


Figure 14: The momentum and angle spectra of charged pions and their correlation from the reaction  $\gamma p \rightarrow \pi^+\pi^+\pi^-n$  for  $8.5$  to  $9.0 \text{ GeV}$  photons (figure taken from reference [31]).

A signature reaction is  $\gamma p \rightarrow n\pi^+\pi^+\pi^-$ , where the  $3\pi$  system has a mass in the range of  $1.5$  to  $2.5 \text{ GeV}/c^2$ . The distributions of charged pions from this reaction are shown in Figure 14. About 50% of these pions are only detected in the FDC. Most of the remainder pass through both the CDC and the FDC, with a tail of particles below about  $1.5 \text{ GeV}/c$  having hits only in the CDC. Other important reactions have larger numbers of pions, (4, 5, 6, ...). As the final state multiplicity becomes larger, the average particle momentum gets smaller, and slower particles are detected at larger angles in the CDC. For the reactions of interest for amplitude analysis, the detector acceptance is sufficient.

The hybrid strangonium states are expected to decay predominantly through several final states that

eventually populate the reaction  $\gamma p \rightarrow pK^+K^-\pi\pi$  [32]. Within this final state, the following reactions are predicted by decay models to be the dominant decay modes.

$$\begin{aligned}\gamma p &\rightarrow pK_1^\pm(1410)K^\mp \\ \gamma p &\rightarrow pK_1^\pm(1270)K^\mp \\ \gamma p &\rightarrow pK^*(892)\bar{K}^*(892) \\ \gamma p &\rightarrow p\phi(1020)f_0(980)\end{aligned}$$

Assuming  $t$ -channel production, the distributions of kaon momentum versus angle are shown in Figure 15 for the four reactions above, where one assume a  $t$  slope of  $\alpha = 5$  and a hybrid mass in the range of 2 to 2.5  $\text{GeV}/c^2$ —in line with all current hybrid predictions [5]. These kaons tend to populate both the FDC and the forward part of the CDC and have momenta from several hundred  $\text{MeV}/c$  up to nearly 6  $\text{GeV}/c$ , with the highest momentum tending to be in the very forward direction. In terms of the ability of GLUEX to reconstruct charged particles, the distribution of physics events is a good match to the geometry of GLUEX.

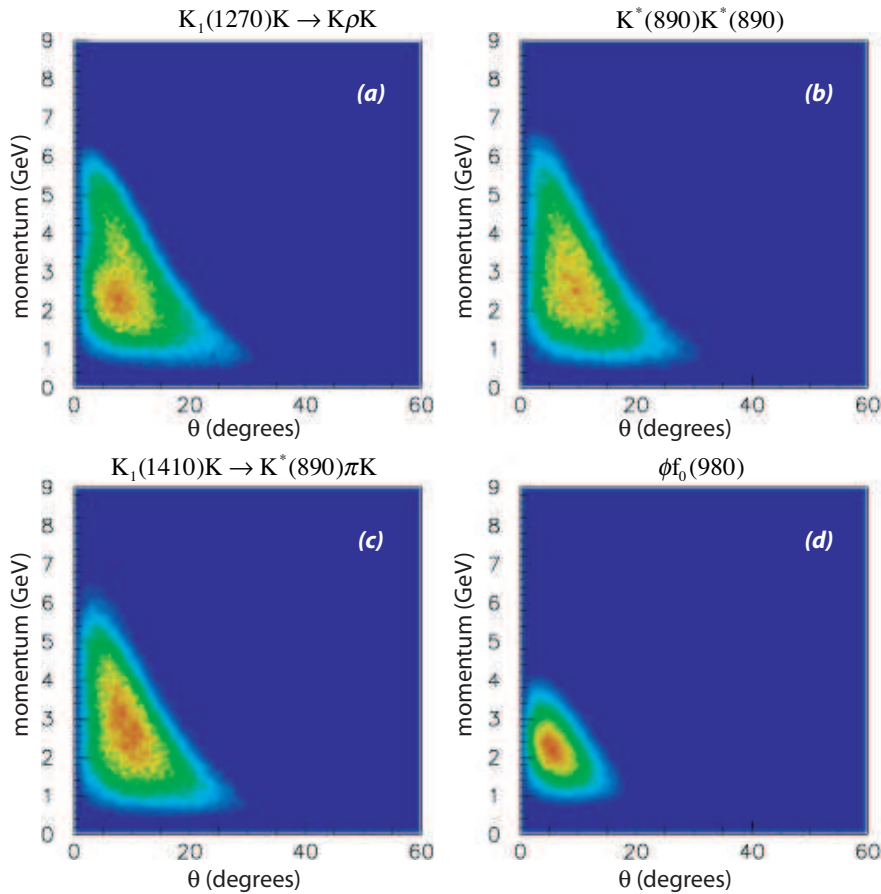


Figure 15: The momentum versus angle (in the lab) for  $K^\pm$  in the reaction  $\gamma p \rightarrow pK^+K^-\pi\pi$  for various intermediate states. (a)  $K_1^\pm(1270)K^\mp p$ ; (b)  $K^*(890)\bar{K}^*(890)$ ; (c)  $K_1^\pm(1410)K^\mp p$ ; and (d)  $\phi(1020)f_0(980)$  (figure taken from reference [31]).

All of the reactions examined above tend to populate the GLUEX tracking system with angles well forward of  $90^\circ$  in the lab. This is true for  $t$ -channel processes where a neutron or proton is connected to the lower vertex—the expected hybrid production mechanism. However, a competing reaction ( $\gamma p \rightarrow \Delta X$ ) can

generate both charged and neutral pions at more backwards angles. In this case, the pion from the decay of the  $\Delta$  can be sent into the backwards direction. Because the CDC can reconstruct charged particles back to at least  $150^\circ$ , the detector will still have good acceptance for these more backwards pions.

## 4.4 Acceptance issues for charged particles

### 4.4.1 The Forward Hole:

The hole in acceptance in the very forward part GLUEX has been defined by background rates in the FDC detectors. The rates at a given position along the beamline specify the minimum active radius of the FDC, with the radius becoming larger as one moves farther downstream. To make the hole uniform in all four FDC packages, the size is defined by tracking  $1 \text{ GeV}/c \pi^+$  through the detector and taking the distance from the beam line in each of the four FDC packages. The result of this is shown in Figure 16. In particular, the first FDC package has a hole that is  $2.3 \text{ cm}$  in radius and the fourth package has a hole that is  $4.6 \text{ cm}$  in radius, (note the mm label in the figure should be cm).

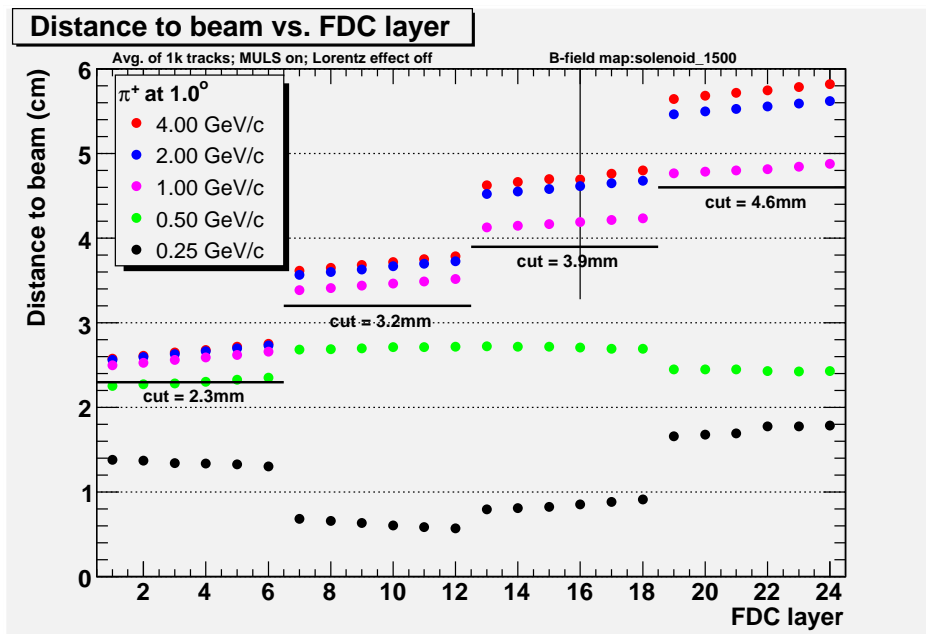


Figure 16: The forward hole near the beamline in the FDC is defined by the requirement that  $1 \text{ GeV}/c \pi^+$  with  $\theta = 1^\circ$  will be measured in the FDC. The plots shows the maximum size of the hole around the beamline in each FDC package  $\pi^+$  particles generated  $1^\circ$  with various values of momentum. The odd structure for  $0.5 \text{ GeV}/c$  and  $0.25 \text{ GeV}/c$  particles occurs due to spiraling of the tracks in the solenoidal field (figure taken from reference [28]). Note that the dimensions of the radial cuts should be labeled as cm and not mm.

As can be seen in Figure 16, the angular size of the forward hole becomes somewhat smaller as the momentum is increased above  $1 \text{ GeV}/c$  and is larger for lower momenta. In particular, the curves that correspond to  $0.25 \text{ GeV}/c$  and  $0.5 \text{ GeV}/c$  show what appears to be an odd structure that is due to the helical trajectory in the magnetic field. Particles with  $0.25 \text{ GeV}/c$  momentum are tangentially approaching the beam axis in FDC packages two and three.

Because decays of hybrid mesons tend to have particles spread out over a large part of the GLUEX detector, the effect of the hole in the forward direction will have very little impact on physics in GLUEX. However, there are reactions where the physics can be impacted by the inability to detect forward-going particles. One particular reaction is diffractive  $\rho$  production.

There have been a number of studies of  $s$ -channel helicity conservation in diffractive vector meson production [11] [33]. Monitoring diffractive  $\rho$  production has been considered as a tool for monitoring the degree of linear polarization of the photon beam for GLUEX. The helicity angles ( $\cos \theta_H$  and  $\phi_H$ ) are the pion decay angles defined in the  $\rho$  rest frame, where the  $\hat{z}$  is taken along the original  $\rho$  direction,  $\hat{y}$  is normal to the  $\rho$  production plane, and  $\hat{x} = \hat{y} \times \hat{z}$ . A study of our ability to use this reaction to cross check our measurements of the photon polarization has been done.

In the study, events were generated assuming  $s$ -channel helicity conservation with a 40% linearly polarized beam at 9 GeV. The acceptance in the helicity angle distributions for a forward angle cut of  $1^\circ$  and  $2^\circ$  is shown in Figure 17. The distortion in the  $\psi_H$  distribution is severe, especially in going from the  $1^\circ$  cut to the  $2^\circ$ . Acceptance corrections can be made, but the knowledge of the efficiency and acceptance as a function of the angular cut have to very well understood to be able to use this as a monitoring tool. Cross checking the measured linear polarization using  $\rho$  decays may well be a challenge. However, because this reaction is very sensitive to how well the acceptance is understood, it will provide an excellent mechanism to test our understanding of the acceptance of GLUEX, which in turn will improve our ability to do an amplitude analysis.

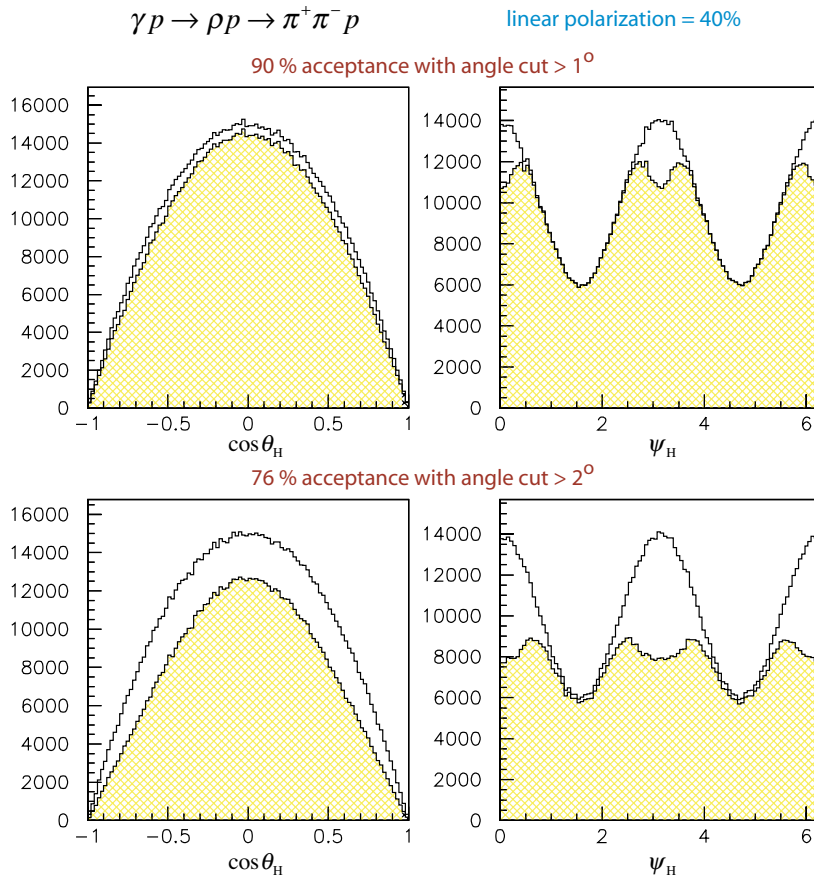


Figure 17: GLUEX acceptance in the  $\rho$  helicity angles assuming 40% linear polarization for the photon beam. The top two plots are for a LAB angle cut of  $1^\circ$  and the bottom two for a LAB angle cut of  $2^\circ$  (figure taken from reference [28]).

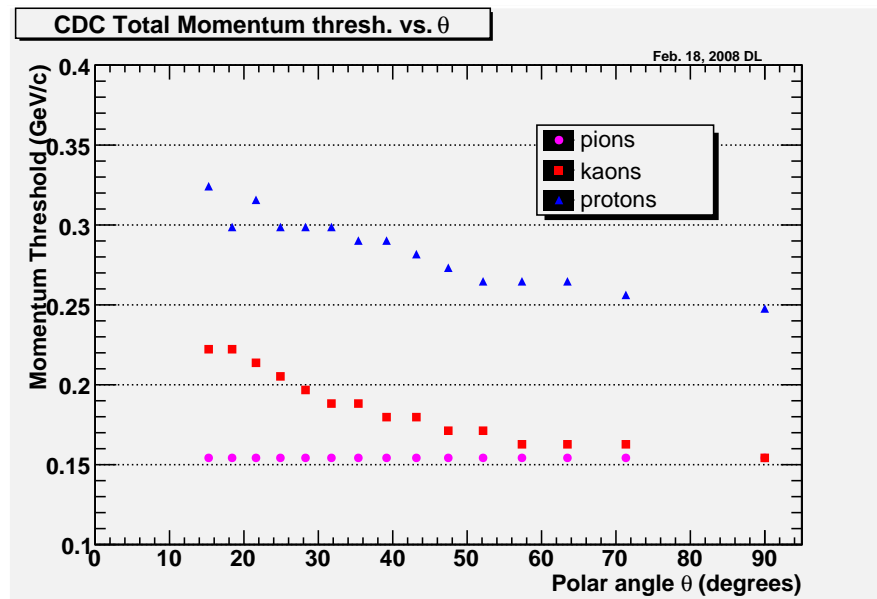


Figure 18: Momentum threshold for reconstructing charged particles in the CDC (figure taken from reference [28]).

#### 4.4.2 Low momentum cutoffs

Monte Carlo studies have been carried out to quantify the low-momentum thresholds for charged particles in GLUEX. These cutoffs are dominated by energy loss in material before reaching the tracking volumes, as well as bending in the strong magnetic field. If we consider particles that traverse the CDC, the cutoff as a function of polar angle from  $15^\circ$  to  $90^\circ$  in the lab and momentum is shown in Figure 18. Pions with momenta smaller than about  $0.15 \text{ GeV}/c$  cannot be reconstructed in GLUEX. For kaons, the cutoff is similar to pions at large angles, but rises to about  $0.22 \text{ GeV}/c$  for forward going  $K$ s. For protons, the cutoff falls from about  $0.33 \text{ GeV}/c$  in the forward directions down to about  $0.25 \text{ GeV}/c$  at  $90^\circ$ . In terms of charged particle reconstruction, the efficiency for detecting slow protons has the biggest effect on the acceptance in GLUEX. Combining this with the information in Figure 13, we see that for mesons systems ( $X$ ) with masses below about  $2 \text{ GeV}/c^2$ , the low- $t$  production will tend to produce a proton that will not be easily detected in GLUEX. These protons will need to be reconstructed using kinematic fitting and missing mass techniques.

### 4.5 Overall performance of GlueX

The resolutions and efficiencies presented in this section ultimately come from a detailed GEANT Monte Carlo of GLUEX and using realistic reconstruction software. These results have then been parameterized and used in section 3 to make comparisons to the performance of Brookhaven E852, an experiment that has carried out precision spectroscopy. It was shown that the performance of GLUEX is comparable to those of E852 and thus, only using comparable statistics as E852, GLUEX should be able to carry out physics analysis to at least the same level of precision.



## 5 Particle identification in GlueX

The lightest members of the spectrum of exotic hybrids will decay predominantly to final states that contain only pions and photons recoiling against either a proton or a neutron. For these particles, the ability to separate pions from protons (and exclude the much less common kaons) will be required. The GLUEX detector has the ability to do this with several  $\sigma$  of separation, and this can be improved by adding kinematic fitting. Ultimately, GLUEX also plans to search for the heavier  $s\bar{s}$  hybrids, where one of the most promising decay modes involves two kaons and two pions. For these later searches, it will be necessary to also identify kaons. For this, the current ability of GLUEX is not nearly as good, however this could be substantially improved with the addition of a Cherenkov detector in the forward direction. In addition to the hardware, we also anticipate sophisticated analysis that will look globally at an individual event to identify the best possible particle assignments consistent with all measured information.

In GLUEX, the PID system consists of the forward TOF wall [29], time-of-flight in the BCAL and  $dE/dx$  information from the CDC. The TOF wall will measure flight times of charged particles in a roughly  $11^\circ$  degree wide cone about the beam axis with 80 ps accuracy. Additional information will come from time-of-flight measurements in the BCAL [30], which are expected to have an accuracy of 200 ps, and possibly from shower profile from charged particles in the BCAL. Finally, the CDC will measure  $dE/dx$  information that will be useful for particles below 0.45 GeV/c momentum. As discussed below, these systems will be able to separate pions from protons in GLUEX. In addition, there will be kaon identification in a limited kinematic region.

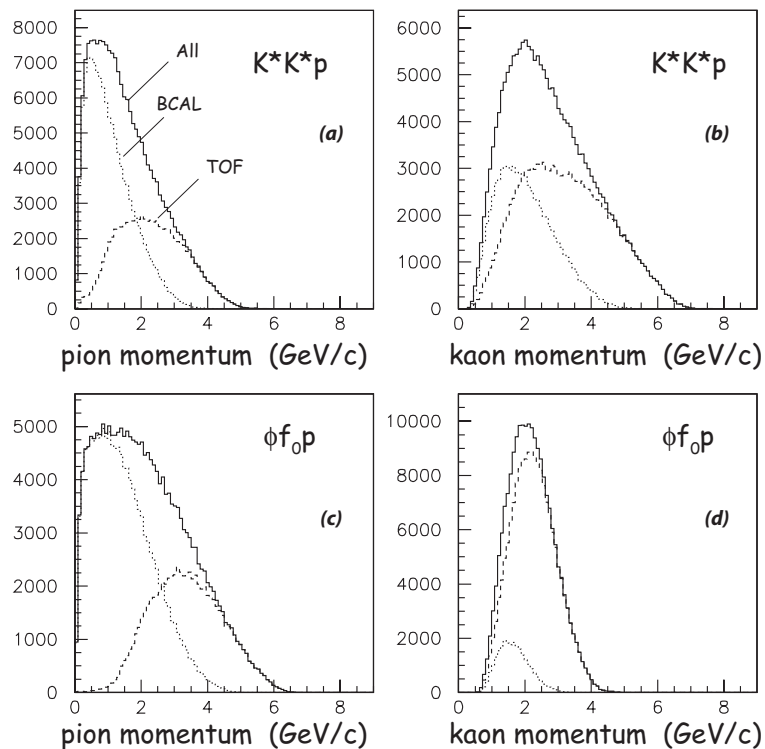
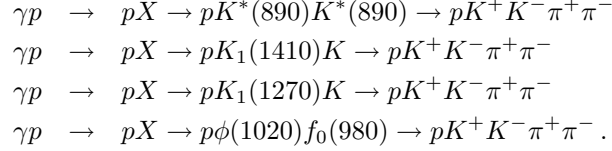


Figure 19: Momentum spectra shown separately for  $\pi^\pm$  and  $K^\pm$  for the final states  $K^*(890)\bar{K}^*(890)p$  and  $\phi f_0(980)p$ . The light dashed histograms are for particle hitting the BCAL and the darker dashed for the forward time-of-flight, while the solid histograms are the sum (figure taken from reference [31]).

## 5.1 Time of flight information

In GLUEX, the reaction  $\gamma p \rightarrow pK^+K^-\pi^+\pi^-$  (see Figure 15) is expected to be one of the best handles on the exotic  $s\bar{s}$  states. Several reactions of interest follow the form:



These reactions have been simulated [31] in the GLUEX detector and the pions and kaons tracked to the BCAL or the TOF. Figure 19 shows the momentum spectrum of the pions and the kaons in both the BCAL and TOF for the first and last of the above reactions.

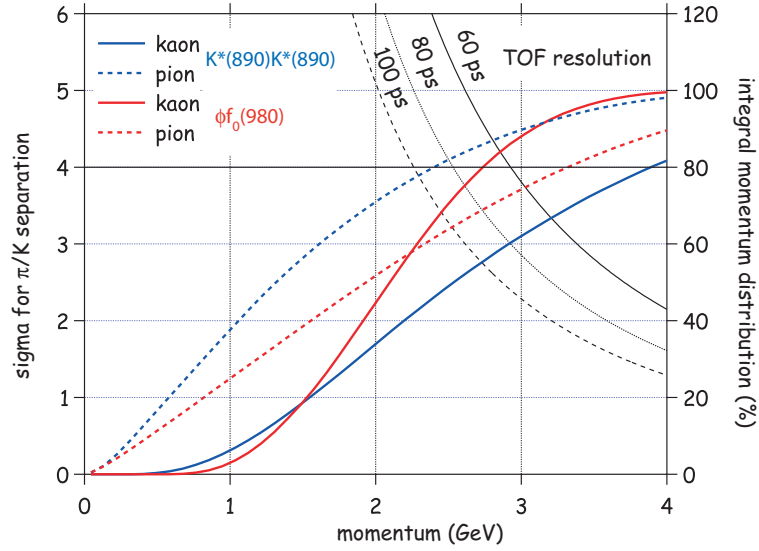


Figure 20: The expected  $\pi/K$  separation using the forward TOF as a function of momentum compared to the integral momentum spectrum. The blue curves correspond to the reaction  $\gamma p \rightarrow pK^*(890)K^*(890)$ , while the red curves correspond to the  $\gamma p \rightarrow pf_0(980)\phi(1020)$ . Both reactions populate the final state  $p\pi^+\pi^-K^+K^-$  (figure taken from reference [34]).

Roughly speaking, particles with a polar angle more forward than  $11^\circ$  will be detected in the TOF wall. With the detector located 5.53 m downstream of the target center, a good approximation for the pion/kaon time difference as a function of momentum is

$$\Delta t = \frac{L}{c} \frac{\sqrt{p^2 + m_K^2} - \sqrt{p^2 + m_\pi^2}}{p},$$

which can be approximated by

$$\Delta t \approx \frac{L}{2cp^2} (m_K^2 - m_\pi^2) = \frac{2071}{p^2} \text{ ps}.$$

This can be used to examine the separation of kaons and pions in the TOF [34]. Figure 20 shows this separation for the first and fourth reaction above. The black curves labeled by timing resolution correspond to the number of  $\sigma$  of separation at the given momentum (read out on the left-hand vertical axis). The colored curves correspond to the integral of the momentum distribution (right-hand vertical scale). A 100 ps

timing resolution would correspond to a  $4\sigma$  separation for pions and kaons for momentum up to 2.5 GeV/c. As the particle momentum begins to rise above about 2 GeV/c, the ability of the TOF wall to separate pions and kaons decreases.

To study the timing in the BCAL [1], we generated events to simulate the reaction  $\gamma p \rightarrow \pi^+ \pi^- \pi^0 n$ , where the  $3\pi$  result from the decay  $a_2(1320) \rightarrow \rho\pi$  or  $\pi_2(1670) \rightarrow f_2\pi$  with a  $e^{-5\cdot|t|}$ . The charged particles were tracked through a uniform magnetic field and for  $\pi^\pm$  reaching the BCAL, the  $\pi/K$  difference was computed (see Figure 21). Clearly, a 200 ps mean-time resolution does not allow for efficient  $\pi/K$  separation in the BCAL. For protons reaching the BCAL, the  $\pi/p$  time difference is also shown. Here, the 200 ps resolution provides very good separation of pions and protons.

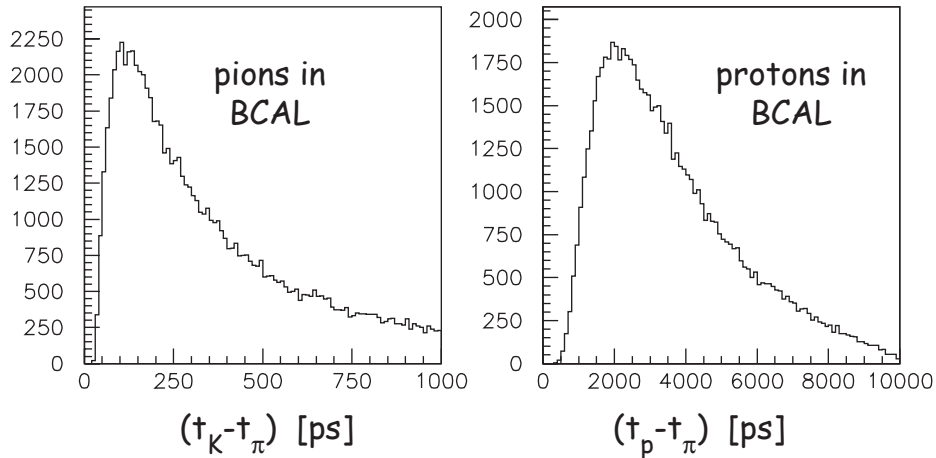


Figure 21: (a) The distribution in pion/kaon time difference for  $\pi^\pm$  reaching the BCAL from the reaction  $\gamma p \rightarrow \pi^+ \pi^+ \pi^- p$ ; (b) the distribution in proton/pion time for the same reaction. The expected time resolution in the BCAL is 200 ps.

The protons from the reactions of interest in GLUEX tend to be observed in the central region of the detector (see Figure 13). While most of these will yield a timing signal in the BCAL, those with transverse momentum smaller than 300 MeV/c will spiral such that they will not hit the BCAL. For those that have low total momentum, a  $dE/dx$  measurement in the CDC may be the only PID measurement that we have. A study of this was performed using the reaction [35]

$$\gamma p \rightarrow p K^+ K^- \pi^+ \pi^- .$$

For this reaction, 90% of the protons were detected in the CDC and 66% of the protons were observed in both the BCAL and the CDC. Placing a  $3\sigma$  cut on the BCAL timing, over 99% of the protons are correctly identified and only 0.2% of the pions leak into the proton sample. For the CDC alone, the  $dE/dx$  is not expected to be quite this good. Here, it is found that 95% of the protons were correctly identified, but 15% of the pions were misidentified as protons. Combining these, GLUEX is expected to have 90% efficiency for identifying protons and a 96% efficiency for rejecting pions. Performing the same study for the kaons, it is found that the signal to background is only about 16%. If GLUEX would only use the individual detectors, an additional factor of about 20 would be needed in  $K/\pi$  separation, mostly in the forward region.

At turnon, the GLUEX detector will be able to separate pions and protons and have some limited capability to identify kaons. The addition of supplementary particle identification such as a RICH detector in front of the TOF wall would allow this to be substantially improved.

## 5.2 Global event analysis

Individual particle identification systems provide a most probable assignment to a particle type based on information in a single detector. Because GLUEX will study exclusive final states, physics principles such as strangeness conservation in conjunction with analysis tools such as kinematic fitting, can be used to make global particle assignments to all particles in an event. Studies with realistic resolutions in GLUEX, in conjunction with kinematic fitting, are currently being carried out [36]. While these have not been fully completed the initial results indicate that improvements by factors of at least a few are possible. Experience from other detectors (such as CLAS) indicate that it is fairly easy to improve by a factor of several over simple particle-based particle identification.

As an example of how kinematic fitting can be applied, one could consider the following two reactions. In addition, one would want to add an appropriate admixture of PYTHIA background events.

$$\begin{aligned}\gamma p &\rightarrow pK^+K^-\pi^+\pi^- \\ \gamma p &\rightarrow p\pi^+\pi^-\pi^+\pi^-\end{aligned}$$

The first is a signature reaction for  $s\bar{s}$  hybrids, while the second is a fairly prolific final state in GLUEX.

When no particle identification is assumed, there are 15 ways to make particle assignments in the final state. All possible assignments would be kinematically fit and cuts on the resulting confidence level would be made. A combination is accepted if it has a confidence level of at least 10% for the correct hypothesis. A hypothesis is rejected if it has a confidence level that is less than 1%. An event would be claimed to be resolved if at the end of the 15 fits, only one hypothesis remained, and it had a confidence level larger than 10%. This can be improved by including a probabilistic identification for each particle based on measurements in the PID system.

In this way, kinematic fitting of exclusive final states can be used to arrive at a global identification of all particles in the final state. If rather than an exclusive final state, one particle is missing, the efficiency of this procedure will drop, but as it uses all available information in conjunction with constraints, it will do better than any individual assignment method.

While it is quite likely that the ability of GLUEX to identify kaons will improve beyond the numbers quoted above, it is still likely that a complete program of strangeness physics will require an additional particle identification detector.

## 6 Conclusions

Photoproduction using linearly polarized photons at  $\approx 9$  GeV is expected to provide a rich hunting ground for exotic mesons. Little data on photoproduction exists at these energies, and that which does exist, provides almost no information on final states with multi-neutrals. Even where data do exist, GLUEX should have statistics that are 4 to 5 orders of magnitude larger. The GLUEX detector has been designed to carry out a broad program in gluonic excitation—a program that will require the complete detection of final states involving charged particles and photons. In addition to tracking charged particles, the analyses need complete calorimetry coverage and uniform acceptance in azimuthal angle around the beamline. The latter is to fully take advantage of the linearly polarized photons. This, coupled with the 9 GeV photon beam, imposes a cylindrical geometry for the detector. We have also shown that in terms of reconstructing quantities relevant to amplitude analysis, GLUEX will perform at least as well as the Brookhaven E852 experiment. The latter demonstrated the ability to carry out high-statistics amplitude analysis and extract signals at the level of a few percent of strong signals. For much of the physics to be performed in GLUEX, separating protons from pions will be essential. Here, we have shown that this can be easily done in GLUEX as designed. The somewhat more difficult task of separating kaons looks to be difficult with the current detector. However, the inclusion of an additional PID element, such as a RICH would, very likely resolve this issue. Overall, the performance of GLUEX will be sufficient to successfully search for exotic mesons in an essentially unexplored reaction.

## References

- [1] A. Dzierba, *et. al*, Physics an Calorimeter Performance metrics. Technical report, GLUEX Document, 2008. GLUEX -doc-985.
- [2] Gunnar S. Bali et al, Static potentials and glueball masses from QCD simulations with Wilson sea quarks. *Phys. Rev.*, D62:054503, 2000.
- [3] Y. Nambu, Technical report, U. of Chicago Report No. 70-70, 1970.
- [4] Nathan Isgur and Jack E. Paton, A Flux Tube Model for Hadrons in QCD. *Phys. Rev.*, D31:2910, 1985.
- [5] Claude W. Bernard *et. al*, Exotic mesons in quenched lattice QCD. *Phys. Rev.*, D56:7039–7051, 1997.
- [6] Thomas D. Cohen, Quantum number exotic hybrid mesons and large N(c) QCD. *Phys. Lett.*, B427:348–352, 1998.
- [7] Eberhard Klempt and Alexander Zaitsev, Glueballs, Hybrids, Multiquarks. Experimental facts versus QCD inspired concepts. *Phys. Rept.*, 454:1–202, 2007.
- [8] Andrei Afanasev and Philip R. Page, Photo- and electroproduction of  $J^{PC} = 1^{-+}$  exotics. *Phys. Rev.*, D57:6771–6777, 1998.
- [9] C. McNeile and C. Michael, Decay width of light quark hybrid meson from the lattice. *Phys. Rev.*, D73:074506, 2006.
- [10] H. H. Bingham *et. al*, Total and partial  $\gamma p$  cross sections at 9.3 GeV. *Phys. Rev.*, D8:1277–1286, 1973.
- [11] J. Ballam *et. al*, Vector meson production by polarized photons at 2.8, 4.7 and 9.3 GeV. *Phys. Rev.*, D7:3150–3177, 1973.
- [12] Y. Eisenberg *et. al*, Photoproduction of  $\omega$  mesons from 1.2 to 8.2 GeV. *Phys. Lett.*, B34:439–442, 1971.
- [13] Y. Eisenberg *et. al*, Study of high energy photoproduction with positron-annihilation radiation. I. Three-prong events. *Phys. Rev.*, D5:15–38, 1972.
- [14] G. Alexander *et. al*, Study of high energy photoproduction with positron-annihilation radiation. II. The reaction  $\gamma p \rightarrow p\pi^+\pi^+\pi^-\pi^-$ . *Phys. Rev.*, D8:1965–1978, 1973.
- [15] G. Alexander *et. al*, Study of high energy photoproduction with positron-annihilation radiation. III. The reactions  $\gamma p \rightarrow p2\pi^+2\pi^-\pi^0$  and  $\gamma p \rightarrow n3\pi^+2\pi^-$ . *Phys. Rev.*, D9:644–648, 1974.
- [16] W.-M. Yao *et. al*, Review of particle physics. *J. Phys.*, G33:1, 2006.
- [17] T. Sjöstrand, S. Mrenna, and P. Skands, Pythia 6.4 Physics and Manual. Technical report, Lund University, 2006. hep-ph/0603175 and <http://www.thep.lu.se/~torbjorn/Pythia.html>.
- [18] A. Dzierba, Comparing Pythia Simulations with Photoproduction Data at 9 GeV. Technical report, GLUEX Document, 2007. GLUEX-doc-856.
- [19] A. Dzierba, Three Pion Production in GlueX. Technical report, GLUEX Document, 2008. GLUEX -doc-1006.
- [20] A. R. Dzierba *et. al*, A partial wave analysis of the  $\pi^-\pi^-\pi^+$  and  $\pi^-\pi^0\pi^0$  systems and the search for a  $J^{PC} = 1^{-+}$  meson. *Phys. Rev.*, D73:072001, 2006.
- [21] D. Lawrence *et. al*, Track fitting in GlueX: Development Report III. Technical report, GLUEX Document, 2007. GLUEX-doc-761.

- [22] A. Dzierba,  $K_S$  Mass Errors Due to Tracking Resolution. Technical report, GLUEX Document, 2008. GLUEX -doc-1007-v1.
- [23] C. .A. Meyer and M. Williams, Kinematic Fiting in CLAS. Technical report, GLUEX Document, 2007. GLUEX -doc-818.
- [24] C. A. Meyer and Y. van Haarlem, The GLUEX Central Drift Chamber. Technical report, GLUEX Document, 2008. GLUEX-doc-990.
- [25] D. S. Carman and S. Taylor, Forward Drift Chamber Technical Design Report. Technical report, GLUEX Document, 2007. GLUEX-doc-754.
- [26] R. T. Jones, Detector Models for GLUEX Monte Carlo Simulation: the CD2 Baseline. Technical report, GLUEX Document, 2006. GLUEX-doc-732.
- [27] D. Lawrence and S. Taylor, GLUEX Simulation Geometry Version 4.0. Technical report, GLUEX Document, 2007. GLUEX-doc-853.
- [28] D. Lawrence, *et. al*, Track Fitting in GLUEX: Development Report IV. Technical report, GLUEX Document, 2008. GLUEX -doc-1004.
- [29] B. Zihlmann, TOF detector description for CDR. Technical report, GLUEX Document, 2008. GLUEX -doc-994.
- [30] A. R. Dzierba, G. J. Lolos and Z. Papandreou, BCAL: Barrel Calorimeter Technical report, GLUEX Document, 2008. GLUEX -doc-986.
- [31] A. Dzierba, A Summary of Kinematics Relevant to the GlueX Experiment. Technical report, GLUEX Document, 2007. GLUEX -doc-883.
- [32] P. R. Page, E. S. Swanson and A. P. Szczepaniak, Hybrid Meson Decay Phenomenology. *Phys. Rev.* , D59:034016, (1999).
- [33] K. Schilling, P. Seyboth, and G. Wolf, On the Analysis of Vector Meson Production by Polarized Photons. *Nuc. Phys.*, B15:397 1970.
- [34] A. Dzierba, PID Introduction and TOF - Talk at March 2007 GlueX Meeting. Technical report, GLUEX Document, 2007. GLUEX -doc-773.
- [35] Eugene Chudakov, (private communication).
- [36] M. Bellis, A study of pi/K separation using the kinematic fitter. Technical report, GLUEX Document, 2008. GLUEX -doc-971.